Journal of Materials Chemistry A

ROYAL SOCIETY OF CHEMISTRY

PAPER

View Article Online
View Journal | View Issue

Cite this: J. Mater. Chem. A, 2023, 11, 18862

New insights on Fe–N–C catalyst structure from valence-to-core X-ray emission and absorption spectroscopies†

Viktoriia A. Saveleva, *[a] Marius Retegan, [a] Kavita Kumar, [b] Frédéric Maillard [b] and Pieter Glatzel [a]

Received 15th May 2023
Accepted 14th August 2023

DOI: 10.1039/d3ta02878j

rsc.li/materials-a

Various spectroscopic techniques have been extensively applied, both *ex situ* and *in situ*/*operando*, to study the structure of the Fe–N–C group of catalysts, promising materials for fuel cell applications. Valence-to-core X-ray emission spectroscopy (VtC XES), a powerful technique to monitor the changes in iron electronic state, is still novel for Fe–N–C characterization. In this work, we analyze the VtC XES spectra obtained on pyrolyzed Fe–N–C catalyst before and after accelerated stress tests in alkaline electrolyte under argon and oxygen atmospheres. By combining both experimental and theoretical spectra, we propose changes in the Fe local geometry after the stress protocols. The observed findings serve as an important contribution to the overall understanding of the FeN_xC_y active sites structures and demonstrate the capabilities of the VtC spectroscopy towards transition metal-based electrochemical systems analysis.

Introduction

In the domain of oxygen electrocatalysis (oxygen evolution or reduction reactions, OER and ORR, respectively), the electron transfer possesses a spin-dependent character.[1,2] In the case of ORR, the reduction of a paramagnetic oxygen molecule to a diamagnetic hydroxide (in alkaline media) or water (in acid) is associated with spin flips in reactants or catalysts. Any changes in the catalyst spin will ultimately affect its catalytic activity by controlling adsorption of reactants and intermediates formation. Specifically, the correlation between metal spin and ORR activity has been demonstrated for iron-nitrogen-carbon (Fe–N–C) electrocatalysts, promising materials for replacing Pt-based catalysts at the cathode of the proton-exchange or anion-exchange membrane fuel cells (PEMFCs and AEMFCs, respectively).[3,4] This catalyst is typically comprised of one or several iron-nitrogen sites embedded into a graphitic carbon matrix (FeN_xC_y with $x = 2$, 3, 4), where their exact structure as well as their location (in-plane, out-of-plane, "bulk"- and "edge"-hosted, *etc.*[3]) depend on the catalyst synthesis route and are still a matter of vivid discussion in the community.[5–7] Apart from FeN_xC_y sites, Fe-based particles, *e.g.*, oxides,[5,8] can be formed during the catalyst synthesis and/or catalyst operation in PEMFCs and AEMFCs. Mössbauer spectroscopy[5,7] and X-ray absorption spectroscopy (XAS) have been extensively applied to characterize these Fe–N–C catalysts both *ex situ*[9–11] and *in situ*/*operando*.[5,12–15] In the case of XAS, where transitions into unoccupied orbitals are involved, the observed features provide information on the geometric and electronic structures of Fe atoms. The X-ray absorption near-edge structure (XANES) region includes the pre-edge and near-edge regions resulting from 1s → 3d and 1s → 4p transitions, respectively, and is sensitive to Fe oxidation state and site symmetry. However, the extraction of this information is tedious and requires complex theoretical calculations with the need for the inclusion of

[a]ESRF – The European Synchrotron, 71 Avenue des Martyrs, Grenoble 38000, France. E-mail: viktoriia.saveleva@esrf.fr

[b]Univ. Grenoble Alpes, Univ. Savoie Mont Blanc, CNRS, LEPMI, Grenoble INP, Grenoble 38000, France

† Electronic supplementary information (ESI) available. See DOI: https://doi.org/10.1039/d3ta02878j

Dr Viktoriia A. Saveleva was awarded her PhD in Physical Chemistry in 2018 at the Univeristy of Strasbourg (France). She has received several awards including Ernst Eckhard Koch Prize from Helmholtz-Zentrum Berlin (2018) and Best PhD Thesis Prize from University of Strasbourg (2019) for her doctoral studies. She was a Post-doctoral Fellow at Electrochemistry Laboratory, Paul Scherrer Institut (Switzerland), and at the beamline ID26 of the European Synchrotron – ESRF (France). Her research contributes to the understanding of the electrocatalysts structure and electrochemical reactions mechanisms using X-ray-based techniques such as photoelectron, absorption and emission spectroscopies.

multiplet structure, core hole potential, or multielectron excitations, thus bear the risk of misinterpretations especially in case of an intrinsically complex and heterogeneous structure of Fe–N–C catalysts. On the other hand, the extended X-ray absorption fine structure region at higher energies resulting from the ionized photoelectron scattering off the electrons of nearby atoms can provide information about the identity of these neighbouring atoms bonded to Fe atoms. In spite of the wide application of this method both *in situ* and *ex situ* towards characterization of the Fe–N–C catalysts structure, one should keep in mind that light element scatterers such as C, N, O, typical ligands surrounding Fe atoms in this material, cannot be easily differentiated. In this case one can apply element-specific X-ray photoelectron spectroscopy,[16,17] however due to typically low concentration of Fe atoms (<1 wt%) as well as their distribution in the "bulk" of the catalyst, the majority of the photoemission signal would originate from the Fe atoms located in the first 5–10 nm from the topmost surface layers, not specifically from catalytically active Fe atoms. Another method, known to be sensitive towards ligand environment is valence-to-core (VtC) X-ray emission spectroscopy (XES).[18–20] Fe XES involves ionization of an 1s electron followed by monitoring the emission of photons during electron decay to fill this core hole, resulting in the $K\beta_{1,3}$ and the $K\beta_{2,5}$ VtC emissions. The $K\beta_{1,3}$ emission is dominated by 3p–3d exchange interaction with a lesser 3p spin–orbit coupling component making it sensitive towards Fe spin and oxidation state,[21,22] while the VtC features stem from the transitions from the filled ligand valence *n*s and *n*p orbitals, respectively, to the Fe 1s core hole, thus probing directly the filled orbitals that are dominantly ligand in nature.[23] Furthermore, modeling of the VtC XES features can be done by considering one-electron transitions within ground-state density functional theory (DFT)[24,25] simplifying the extraction of the useful information in comparison to complex calculations of a full XANES spectra.

This work presents a study of Fe–N–C catalyst structure using Fe VtC XES. Metal–organic framework-derived catalyst Fe0.5 (labelled as $Fe_{0.5}$RP in previous publications),[5,26] comprising exclusively atomically-dispersed Fe in a N-doped carbon matrix (FeN_xC_y-sites), have been previously extensively investigated using electrochemical and numerous analytical methods before and after accelerated stress tests (ASTs) in a three-electrode liquid electrochemical cell.[27] Briefly, two ASTs composed of 10 000 cycles between [0.6–1.0] V_{RHE} in O_2- or Ar-saturated 0.1 M NaOH electrolyte at 60 °C, referred as AST O_2 and AST Ar, respectively, have been applied to Fe0.5-based catalyst layers (CLs) deposited on a glassy carbon electrode. Irrespective of the gas atmosphere, we observed the following changes in the aged samples: (i) slight drop (*ca.* 10%) in the ORR activity; (ii) decrease in Fe content due to partial Fe dissolution from FeN_xC_y-sites (*ca.* 50%) into the electrolyte, where *ca.* 15% of dissolved Fe was precipitated in the form of iron oxide Fe_xO_y and/or oxyhydroxide $FeO(OH)_x$; (iii) mild corrosion of the carbon matrix.[27] Based on these findings, we related the maintained ORR activity possibly to a synergetic effect between formed iron oxide/hydroxide particles and the FeN_xC_y sites present in the CL after the ASTs. In this work, we focus on the state of Fe before and after the ASTs. In order to exclude any artefacts related to the catalyst storage conditions[28] between previous and current measurements, we repeated the ASTs on a freshly prepared Fe–N–C catalyst and its CLs, respectively. The resulted CLs are analysed using Kβ high-energy resolution fluorescence detected (HERFD) XANES and XES including the VtC region. The analysis of the VtC XES data was carried out with the aid of density functional theory (DFT), where the spectra were calculated for several FeN_xC_y and $FeN_xC_y(OH)_z$ structural models with varying Fe electronic spin state. Additionally, we describe the variations in the spectral intensities in terms of molecular orbitals contributions.

Experimental

Catalyst layer preparation and accelerated stress tests

Fe0.5 electrocatalyst was synthesized *via* ramp pyrolysis synthesis of Fe(II) acetate, 1,10-phenanthroline and metal-organic framework precursor mixture at 1050 °C, the details can be found in Zitolo *et al.*[29] Fe0.5-based electrodes were prepared by drop-casting onto a glassy carbon disc of an 20 μL aliquot of the catalyst suspension (10 mg of Fe0.5 catalyst; 50 μL of 5 wt% Nafion solution, Sigma-Aldrich; 854 μL of isopropanol, Carl Roth; 372 μL of Milli-Q grade water). The catalyst loading is 0.8 $mg_{Fe0.5}$ cm^{-2}. The ASTs were performed in a polytetrafluoroethylene cell at 60 °C. A commercial reversible hydrogen reference electrode (RHE, Hydroflex, Gaskatel GmbH) connected to the cell *via* a Luggin capillary and a glassy carbon plate were used as reference electrode and counter electrode, respectively. 0.1 mol L^{-1} NaOH electrolyte (Alfa Aesar) was purged with Ar and O_2 gas (Messer), $Fe_{0.5}$ electrode was cycled in the potential range 0.6 and 1.0 V_{RHE}, in total 10 000 cycles were performed. More details on the experimental procedure can be found in our previous work.[27]

$Fe(OH)_3$ reference sample was prepared by precipitation method. 1 g $FeCl_3 \cdot 6H_2O$ (Sigma-Aldrich, ACS 97%) was added to 20 mL Milli-Q grade water, followed by 10 mL 4 M NaOH (Sigma-Aldrich, Suprapur, 99.99%). A brown precipitate was formed, filtered, and washed three times with water. The powder was then air-dried overnight at 60 °C. The obtained $Fe(OH)_3$ was measured in the form of a pellet mixed with cellulose.

Fe Kβ HERFD XANES and XES measurements

Fe Kβ HERFD XANES and XES measurements on the glassy-carbon-supported Fe0.5-based catalyst layers were carried out at beamline ID26 of the European Synchrotron – ESRF (Grenoble, France). The data were recorded in air at room temperature. The storage ring operated in 7/8 multibunch mode with an electron current of 196 mA. Three undulators produced the incoming radiation, which was monochromatized by a pair of Si (111) crystals, cryogenically cooled. The energy calibration of the incident beam was achieved using a reference metallic iron foil by setting the first inflection point of Fe K edge to 7112 eV. Kβ HERFD XANES spectra were collected in a continuous scan mode by varying the

incident energy from 7080 to 7250 eV across the Fe K edge with an energy step 0.1 eV and duration of 60 seconds, where each XANES scan was taken on a fresh spot, not previously exposed to the X-ray beam. The maximum of the Fe Kβ fluorescence line (7059 eV) was selected with an emission spectrometer in Rowland geometry with three Ge (620) analyser crystals ($R = 1$ m) aligned at Bragg angle of 79.09°. The emission spectrometer was aligned using the elastic peak at Kβ fluorescence energy. A Si avalanche photodiode with 200 μm thickness and 10×10 mm^2 active area was used as a detector. The dead time correction was performed using a nonparalyzable model with $\tau = 3.99 \times 10^{-8}$. Kβ XES spectra were recorded as a multirange scan with 4 intervals varying the step size and acquisition time: (1) Kβ mainline region (7030–7070 eV) was recorded with a step size of 0.1 eV and acquisition time of 1 s per point; (2) 1st transition region (7065–7085 eV) with a step size of 2 eV and acquisition – 1 s per point; (3) VtC region (7085–7125 eV) with a step size of 0.1 eV and 5 s per point acquisition time; (4) 2nd transition region (7125–7135 eV) same as the 1st transition. The obtained spectra were interpolated on the energy range of 7030–7135 eV and a full XES spectrum was used for background correction (see Results and discussion, Fig. S1†). The incident energy of 7800 eV was used to collect XES spectra based on the previous study.[30] The beam damage after collecting a full XES scan was controlled by XANES spectra recorded before and after at the same spot on the sample. At least 2 Kβ XES scans were collected for each sample. The beam stability of the analysed catalysts has been investigated during our previous experiments in ref. 11 and 27. Both HERFD XANES and XES spectra were normalized to the incoming flux recorded by detecting the scattering from a Kapton foil with a photodiode and then were normalized in area using the full measured energy range. Data treatment was performed using Python-based scripts.

VtC XES calculations

The VtC XES calculations were done using the ORCA 5.0.0 quantum chemistry software package.[31] We used the BP86 density functional.[32] The scalar relativistic effects were treated using the ZORA Hamiltonian[33] and the relativistically contracted def2-SVP basis set for carbon and hydrogen, and the def2-TZVP basis set for the remaining atoms.[34] The resolution of identity was used to speed up the calculations together with the SARC basis sets.[35,36] Dispersion correction was included using the Becke–Johnson damping.[37] The solvent effects were included using the CPCM model with water as a solvent.[38] Subsequent frequency calculations were used to verify that the optimized structures were minima on the potential energy surface. The VtC XES spectra were calculated using the same theoretical methods used during the geometry optimizations. Input files for structure optimization, frequency calculation, and XES spectra calculations are provided in the ESI.† It should be mentioned that the absolute energy scale of the calculated spectra deviates from the experimental ones; however the relative energy scale can be used for the data analysis.[39] To facilitate the direct comparison with the experimental data, all calculated spectra were shifted by 60 eV.

Results and discussion

Experimental XANES and XES data

Fe Kβ HERFD XANES spectra recorded on pristine and post-mortem Fe0.5-based CLs, before and after the ASTs, respectively, are reported in Fig. 1a. XANES signature of Fe0.5 catalyst is similar to the ones presented in literature for the same type of catalyst[9,26,29] and possesses characteristic features of FeN_xC_y sites. The spectra are also similar to the ones reported in Sgarbi *et al.*[27] where small discrepancies can be related to different synthesis batch of the $Fe_{0.5}$ catalyst used in our previous and current works and/or a longer storage of the former batch prior to the synchrotron measurements in comparison to a freshly synthesized and analysed in the current manuscript resulting in slightly different catalyst initial structure. The comparison of the spectra obtained on the CLs before and after the ASTs presented in Fig. 1 does not reveal any significant differences neither in the position of the main edge nor in the pre-edge region. Increase in the intensity of the white line after the ASTs can be related to the changes in the Fe–N bond length, while overall coordination of Fe is maintained after the ASTs based on the unchanged pre-edge features.

While XANES probes unoccupied states, XES as a secondary optical process provides information on the occupied states of Fe, where specifically Kβ emission lines are mainly shaped by intra-atomic interactions between 3p and 3d spin-unpaired electrons. The Kβ mainline (7030–7070 eV) arises from 3p → 1s transitions, where the 3p–3d exchange interaction splits it into low-energy Kβ′ (7035–7050 eV) and high-energy $K\beta_{1,3}$ features (7055–7065 eV) making them spin sensitive.[22,40] The Kβ spectra of the analysed CLs are shown in Fig. 1b. While there are little or no changes in XANES data after the ASTs, we notice a blue shift and a reduction of the $K\beta_{1,3}$ peak accompanied by the rise of the Kβ′ low energy peak in the aged samples. These changes are typically assigned to increase in average spin state of Fe atoms.[21,22] Such a change in the Fe electronic state correlates with local geometry perturbations, namely bond length and angles. The VtC region of XES (7085–7125 eV) divided in low energy Kβ″ (7085–7095 eV) and main $K\beta_{2,5}$ (7095–7115 eV) lines, corresponds to the transitions of valence molecular orbitals with s- and p-ligand character, respectively, making them sensitive to the identity and electronic structure of the bonded ligands.[41,42] Fig. 1c presents background subtracted VtC spectra of pristine and aged Fe0.5-based CLs. The background subtraction was done according to the procedure described in ref. 41. Fig. S1† shows an example of its modelling using three pseudo-Voigt functions. Fig. S2† presents the VtC XES spectra obtained on the Fe0.5-based CLs analysed in our previous publication.[27] The degree of changes is different for two batches studied previously and in the current work, however we observe the presence of the same peak at the energies above the main $K\beta_{2,5}$ peak after the ASTs in Ar and O_2.

In our previous work, we provided transmission electron microscopy (TEM) evidences of partial leaching of Fe atoms

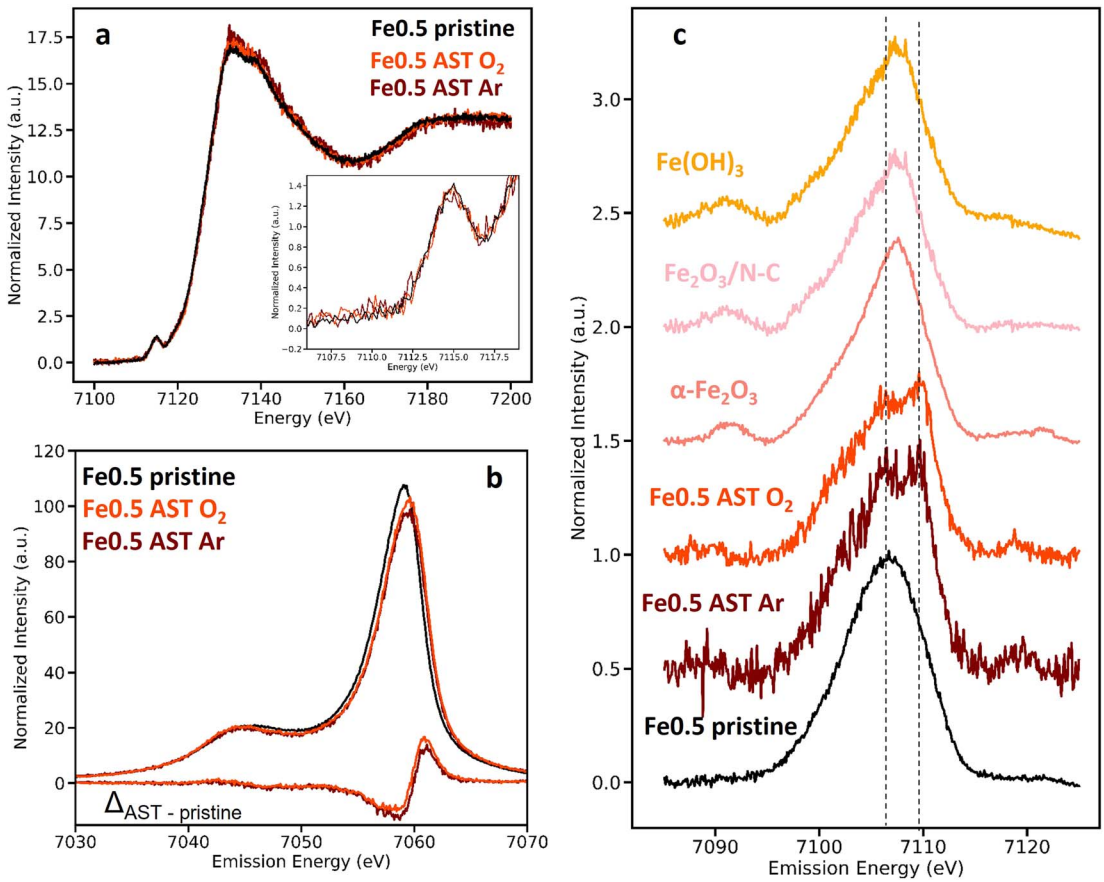

Fig. 1 Fe Kβ HERFD XANES (a), Kβ mainline (b) and VtC XES spectra (c) obtained on Fe0.5-based electrodes before and after the ASTs. Panel c also contains VtC spectra for bulk and nano-sized Fe_2O_3 as well as $Fe(OH)_3$ references. The VtC signals have been vertically shifted for the sake of clarity.

from Fe–N coordination followed by their precipitation in the form of Fe_xO_y/$FeO(OH)_x$ nanoparticles during the ASTs.[27] Interestingly, the presence of iron oxide nanoparticles in the aged CLs could also explain the growth of Fe average spin observed in this work. In order to verify if the formation of these nanooxides/hydroxides may result in the new features observed in the VtC of AST O_2 and AST Ar samples, we collected the VtC spectra on a commercial bulk α-Fe_2O_3 powder (CAS number: 1309-37-1), nano-sized Fe_2O_3 particles (6–8 nm based on the TEM images) deposited on a N-doped carbon (Fe_2O_3/N–C)[5] as well as $Fe(OH)_3$ powder (Fig. 1c). In spite of different particles size, the VtC signatures of both iron oxides resemble each other. Moreover, their signal is also similar to the one obtained on iron hydroxide powder possessing a well-resolved Kβ″ peak at *ca.* 7092 eV originated from Fe–O ligand. The spectra obtained on the aged Fe0.5-based CLs also contain a Kβ″ peak, however at lower energy of *ca.* 7090 eV. The 2 eV energy difference can be related to a difference in ligand type or a different form of oxygen-based ligand.[19] Interestingly, a pristine CL does not show any Kβ″ feature. The position of the main $K\beta_{2,5}$ line obtained for Fe_2O_3 (7107.5 eV) is shifted towards the higher energies by 1 eV in comparison to pristine Fe0.5-based CL. The value is lower than the position of the additional feature at 7110 eV observed on the higher energy side of the $K\beta_{2,5}$ in the CLs after the ASTs. Thus, the formation of iron-based nanoparticles observed previously in TEM cannot explain the changes in the VtC signature of the aged samples Fe0.5 AST O_2 and Fe0.5 AST Ar. That can be explained by another iron oxide structure that is different from the benchmark Fe_2O_3 probed here. Furthermore, the presence of Fe oxide/hydroxide nanoparticles in the aged samples would also influence Fe pre-edge shape and intensity that is not observed in the experimental spectra (Fig. 1a). In our following discussion we assign these new features observed in the VtC spectra of the aged samples to the changes in the FeN_xC_y-sites structure that are further analysed using DFT calculations.[43]

According to earlier studies, $Fe_{0.5}$ catalyst powder contains two square planar (D_{4h}) FeN_xC_y sites of different Fe coordination environment, usually referred to as pyridinic and pyrrolic structures.[5,26] Additionally, in our recent publication we have shown that preparation of the electrodes based on this material triggers partial formation of octahedral (O_h) sites by adding two axial oxygen-based groups resulting in co-existence of 4- and 6-coordinated sites in the final CL.[11]

It is well-known in electrocatalysis that not all the catalytic sites are electrochemically active, *i.e.* they do not all respond to

the applied potential bias. Moreover, beforehand these sites should be accessible by the electrolyte in order to form a three-phase boundary, while part of the FeN_xC_y sites can be located in the bulk of the catalyst and or in micropores (with size <2 nm) or closed pores. We thus hypothesize that a fraction of one or both FeN_xC_y sites present in the $Fe_{0.5}$ catalyst initially would be affected by the potential cycling during the ASTs applied in this work, while all Fe species contribute to the collected XANES and XES spectra shown in Fig. 1. Due to the current absence of any reliable method to quantify the amount of the electrochemically-active FeN_xC_y sites as well as unknown exact initial structure present in Fe0.5 catalyst, we refrained from attempting any quantitative analysis of the data presented here,[44] and focus only on the relative comparison of the experimental and calculated VtC spectra. Specifically, by varying the electronic structure of Fe, we aim to reproduce the high energy component of the $K\beta_{2,5}$ peak, as well as the $K\beta''$ intensities formed after the ASTs.

Selected FeN_xC_y structures

According to the current understanding of the ORR on the molecular MeN_4 (Me = transition metal) catalysts, its mechanism includes either $2e^-$ + $2e^-$ or $4e^-$ electron transfer depending on the oxygen binding energy.[45] In case of $Fe_{0.5}$ catalyst in alkaline media (except for strong base solutions with pH = 14), the ORR follows predominantly a $4e^-$ path, where the reaction can be described as:

$$O_2 + 2H_2O + 4e^- \rightarrow 4OH^-$$

Thus, the potential cycling in alkaline electrolyte in the presence of O_2 may lead to the formation of 5- or 6-coordinated sites containing one or two OH^- axial ligand(s). In case of the ASTs in the presence of Ar gas, where no oxygen molecule is available for the ORR, FeN_xC_y sites may also adsorb OH^- groups from the electrolyte solution.

The development of representative structural models of the catalyst's active iron-nitrogen sites before and after the ASTs is complicated as the details regarding the coordination environment, the spin and oxidation state of iron are lacking. As such, the number of models can quickly increase if no limits are set on the variations considered. To avoid having to calculate an unreasonably large number of models, which would be computationally demanding but also challenging to analyse, we limit the possible nitrogen-based coordination environment to FeN_4C_{10}, pyridine-type site where FeN_4 is a "bulk"-hosted site surrounded by 10 carbon atoms and integrated in a graphene sheet; FeN_4C_{12}, pyrrolic-type site, where FeN_4 site is surrounded by 12 carbon atoms; FeN_4C_7, "edge"-hosted pyridinic site with 7 carbon atoms, respectively.[9,29] The main difference between the two pyridinic sites FeN_4C_{10} and FeN_4C_7 is the location of the FeN_4 group, inside of the graphene plane or at its edge, respectively. Both "bulk"- and "edge"-hosted FeN_xC_y sites may be present in the pristine catalyst Fe0.5. For all models, we also consider, in addition to the case where no additional ligands are coordinated, square-pyramidal models (C_{4v}) with one coordinated hydroxyl ligand and octahedral models (O_h) having two axially coordinated hydroxyl groups consistent with our previous study on Fe–N–C catalyst layer preparation.[11] In total, we selected nine structural models presented in Fig. 2. For each of these models, we explored three spin states for iron, low spin, intermediate spin, and high spin, for both oxidation states, 2+ and 3+. We considered two formal oxidation states as we cannot fully exclude the presence of one oxidation state or another based on the current understanding of the Fe–N–C materials and the analytical methods applied to characterize them. The size of the model was selected to be big enough for a proper representation of the real sites structure keeping the calculation time reasonable. In total we have optimized 54 structural models listed in Table S1.† We have ensured that all models are in local minima on the potential energy surface using frequency calculations. In addition, the calculations provide an estimate of the Gibbs free energy (G) which was used to select the thermodynamically favorable spin state of iron for a given coordination and iron oxidation state. In the following we focus the discussion mainly on the XES spectra of the models having the lowest G among the three spin states. As we expect the calculated ΔG values to be rather sensitive to the density functional used, in a few highlighted cases, we also discuss the spectra of models that are higher in energy.

In the following, we analyse and compare the calculated VtC spectra representing two possible scenarios that may take place during the ASTs in alkaline electrolyte both in Ar and O_2 atmosphere: (1) transition from 4- to 5-coordinated iron-nitrogen sites *via* adding an axial OH^- group; (2) change in "bulk"- and "edge"-hosted FeN_xC_y sites relative concentrations.

Formation of 5-coordinated FeN_xC_yOH sites

The potential cycling of the Fe0.5-based electrodes may promote additional adsorption of one or two axial OH^- group(s) on Fe atoms regardless of the gas (oxygen or argon) that was purged through the electrolyte, leading to the formation of either square-pyramidal or octahedral sites, respectively. We consider transitions to 6-coordinated octahedral sites to be less likely as an increase in their concentration at the expense of the four-coordinated sites would affect the pre-edge of Fe K edge spectra after the ASTs, which is not the case (*cf.* Fig. 1). In contrast, due to a small difference in the intensity of the pre-edge region for the 4- and 5-coordinated Fe sites,[46] the addition of a single OH^- group to some FeN_xC_y sites would not contradict experimental XANES data. In contrast, the additional oxygen-based ligand in the coordination environment of iron leads to specific changes in the calculated XES VtC spectra; the $K\beta''$ region shifts to higher energy and is more intense, while at the $K\beta_{2,5}$ region, we observed the formation of a shoulder at approximately 4 eV above the main peak (Fig. 3). Next, we will discuss the origin of the observed changes in terms of the orbital contributions for the Fe^{2+} pyridinic "bulk"-hosted models, FeN_4C_{10} and $FeN_4C_{10}(OH)$. We note, however, that similar changes are observed in the XES VtC spectra upon coordination of an OH^- ligand, regardless of the oxidation state and initial coordination environment of iron.

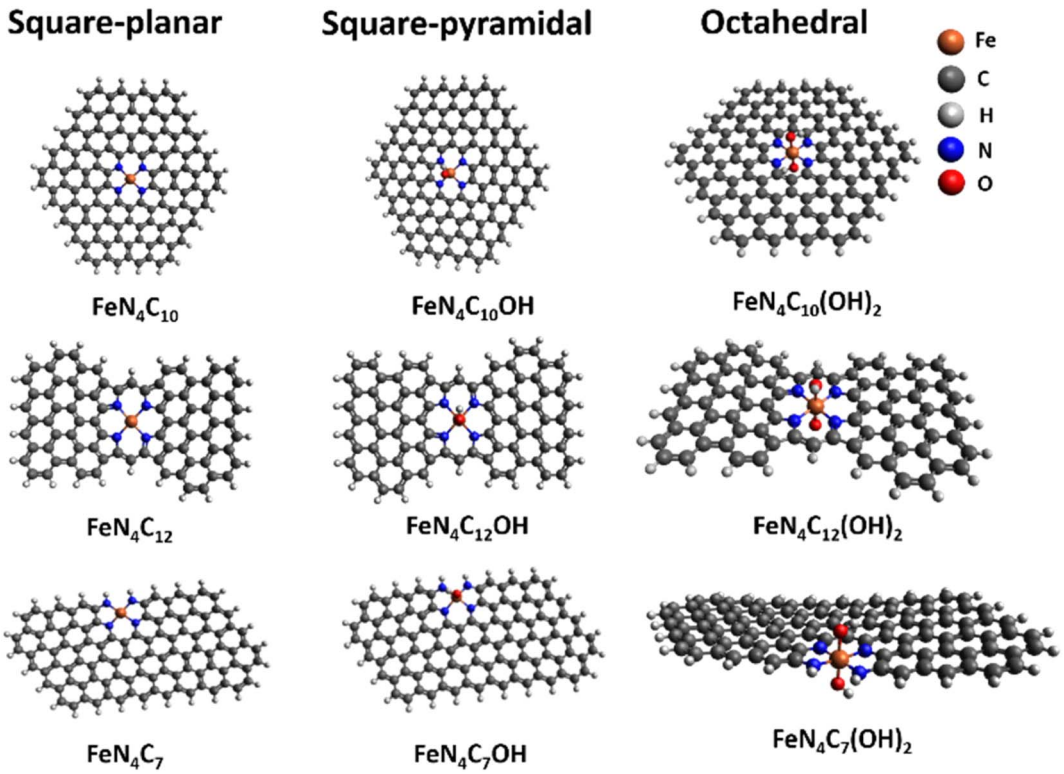

Fig. 2 FeN_xC_y model structures used in this work.

Fig. 4 highlights several key MOs contributing to the observed changes in the calculated VtC spectra of the two models, FeN_4C_{10} (Fig. 4a) and $FeN_4C_{10}OH$ (Fig. 4b). The intensity of the Kβ″ is governed by the amount of metal *n*p mixing into the ligand-centered s-based molecular orbitals, where the energy of this feature is related to the ligand

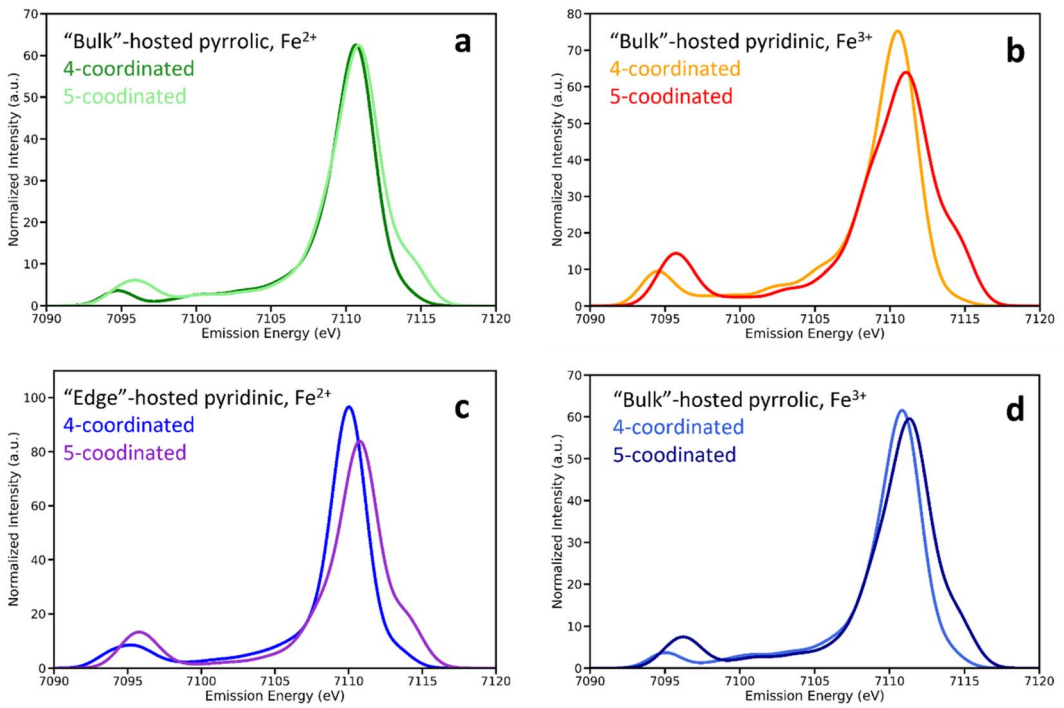

Fig. 3 Comparison of the theoretical VtC XES spectra for 4-coordinated FeN_xC_y and 5-coordinated FeN_xC_yOH bulk pyrrolic (a and d) and pyridinic (b and c) sites. Fe oxidation state is provided in the panels.

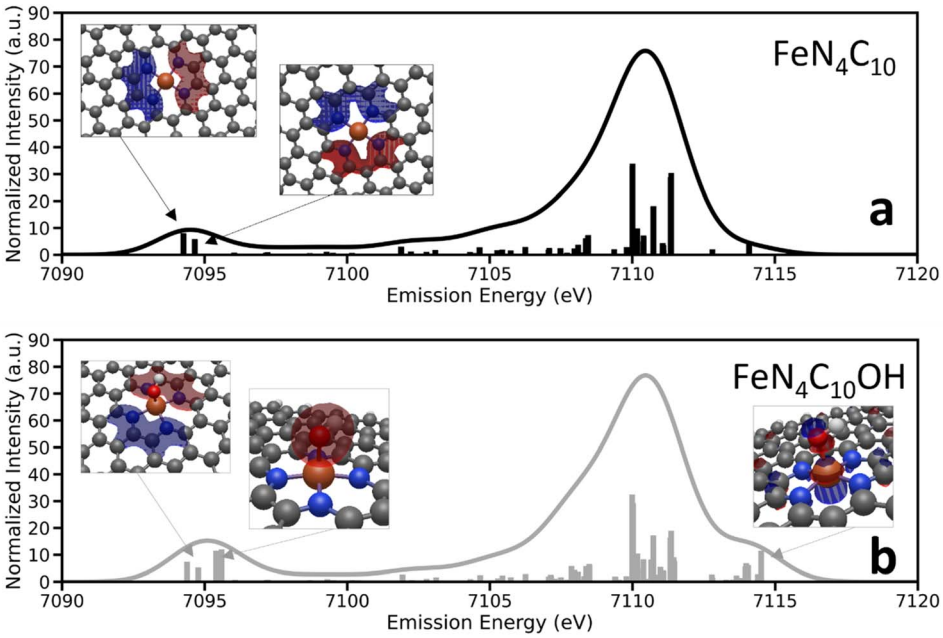

Fig. 4 Calculated VtC XES spectra for FeN_4C_{10} (a) and $FeN_4C_{10}OH$ (b) sites and representative molecular orbitals giving rise to some of the transitions.

ionization potential. For both models, we observe two sets of transitions between 7094 and 7095 eV involving MOs with contributions from the pyridinic groups, primarily N based, that are observed in both panels of Fig. 4. At higher energy, two additional transitions can be observed for $FeN_4C_{10}OH$ (Fig. 4b) that involve the spin-up and spin-down MOs, comprising the majority s-based oxygen and hydrogen-based contributions that sum up to approximately 81% of the MOs. These additional transitions, which appear 1 eV above the ones involving the in-plane ligands, and which are of slightly higher intensity, lead to the observed overall changes of the Kβ″ feature. A similar orbital analysis of the two intense transitions making the high-energy shoulder of the $K\beta_{2,5}$ line observed following the addition of the OH^- ligand, reveals that they originate from the anti-bonding MOs involving the metal d-orbitals and oxygen p-orbitals. As with Kβ″, the energy position of the $K\beta_{2,5}$ features is indicative of the ligand nature (N *vs.* O), as these transitions are sensitive to the changes in the ionization energy of the MOs.[25]

"Bulk-" *vs.* "edge"-hosted sites

Fig. 5 compares the VtC signatures calculated for 4-, 5- and 6-coordinated pyridinic sites located either at the edge of the graphene layer, "edge"-hosted ones, or in the middle of it – "bulk"-hosted sites (see model structures in Fig. 2). The data are also provided for two oxidation states of Fe atom, +2 and +3. For all structural models analysed here, we see the same blue shift of "edge"-hosted sites in comparison to the "bulk" ones. The intensity of the Kβ″ feature is almost identical due to the same ligands surrounding Fe atoms, however there is also a difference in the energy position of this feature depending on the location of the FeN_xC_y site. Similar to the $K\beta_{2,5}$ line, the Kβ″ is shifted in the same direction and by the same value, *i.e.*, the energy gap between Kβ″ and $K\beta_{2,5}$ remains constant regardless the site placement in the graphene. The latter can be also related to the same atoms attached to Fe, where it is known that the energy position of the Kβ″ depends on the ligand nature.[19]

Recent dissolution studies performed on a similar Fe0.5 catalyst during the ASTs close to the ones used in this work demonstrated that Fe demetallation from the FeN_xC_y sites can be a main cause of Fe leaching in alkaline media.[47] Additionally, Ma *et al.* showed that "edge"-hosted FeN_xC_y sites tend to be more active towards the ORR and stable in comparison to the catalyst comprising predominantly "bulk" sites.[48] The former was also confirmed by other research groups.[49,50] Based on these and our previous findings on the changes in the Fe0.5 catalyst properties after the ASTs (*ca.* 50% loss of Fe from the FeN_xC_y sites; maintained ORR after the ASTs, ref. 27), we propose a partial demetallation of Fe atoms from "bulk"-hosted FeN_xC_y sites exposed to the electrolyte and responding to the applied potential, *i.e.* electrochemically active ones, where more stable "edge" ones are responsible for maintaining the ORR activity after the stress protocols. In other words, the ratio between "bulk" and "edge" sites initially present in the Fe0.5-based CL decreases after the ASTs in both Ar and O_2 atmospheres. From the calculated VtC spectra (*cf.* Fig. 5), we see that independent on the Fe coordination number the "edge"-hosted sites possess a 2 eV higher $K\beta_{2,5}$ line than the ones located in the "bulk". Thus the increase in the "edge" sites concentration after the stress tests results in a higher intensity of their $K\beta_{2,5}$ feature accompanied by the decrease of the feature related to the "bulk" ones and gives rise to the high-energy shoulder observed in the experimental VtC data after the ASTs.

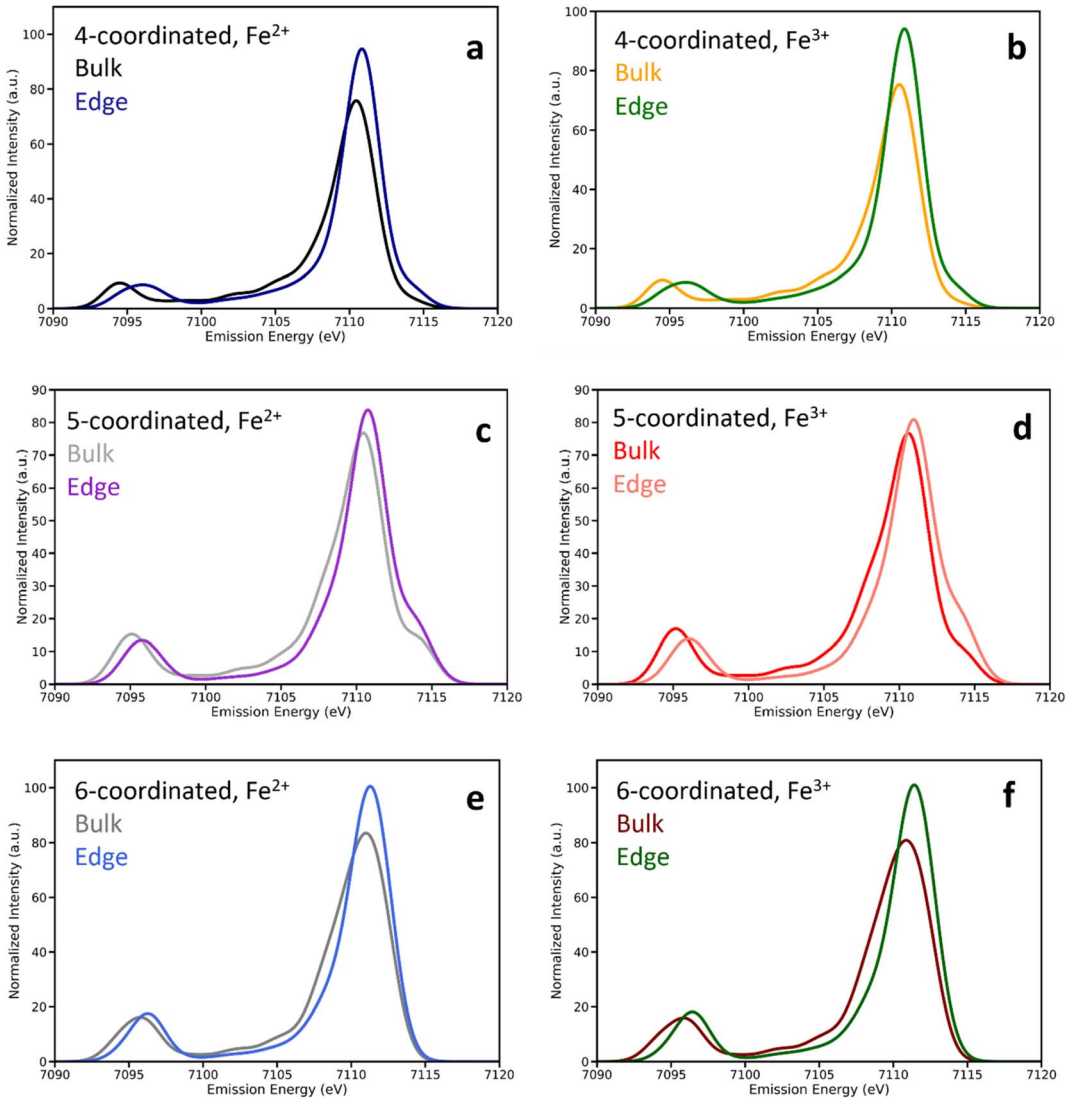

Fig. 5 Calculated VtC XES spectra for bulk- and edge-located pyridinic 4-coordinated FeN_xC_y (a and b), 5-coordinated FeN_xC_yOH (c and d) and 6-coordinated $FeN_xC_y(OH)_2$ sites (e and f). Two oxidation states of iron atoms Fe^{2+} (a, c, and e) and Fe^{3+} (b, d, and f) are compared.

In summary, we propose that the ASTs applied to Fe0.5-based electrodes may lead to one or both structural changes: (i) square planar (FeN_xC_y) → square pyramidal transition (FeN_xC_yOH) by adding one axial OH^- ligand during potential cycling; (ii) increase in "edge"-/"bulk"-hosted sites ratio as a result of preferential Fe dissolution from the "bulk" sites. Interestingly, that in both cases, either the formation of 5-coordinated sites from 4-coordinated or higher fraction of "edge"-hosted sites in comparison to "bulk" ones, the structures formed in the CLs after the ASTs possess higher spin population (see Table S1†) than the ones in the pristine CL. This is in line with the experimental Kβ mainline data, from which we conclude an increase in average spin of Fe after the stress tests.

Conclusions

Here we demonstrate the possibilities of the VtC XES coupled with theoretical calculations to provide unique information on the structure of the Fe–N–C catalysts by analysing the changes in their spectral signature before and after the ASTs in alkaline media. The XES VtC spectra of several FeN_xC_y sites with and without axial OH^- ligand(s) are modelled using DFT as implemented in the ORCA code and compared with the ones obtained experimentally. Based on these findings, after the ASTs we propose the formation of square-pyramidal FeN_xC_yOH structures and decrease in the "bulk"-/"edge"-hosted sites ratio. We also suggest that the "edge" sites can be responsible for nearly maintained ORR activity after the stress tests. This work paves the way for using VtC XES to study the Fe–N–C catalysts and provides new opportunities for its *operando* application.

Author contributions

V. A. S., K. K, and F. M. conceived and initiated the project, K. K. prepared the catalytic layers and ran the accelerated stress tests, V. A. S. performed XAS and XES measurements, V. A. S.

and M. R. performed DFT calculations, P. G., K. K., F. M., and M. R. were involved in the data analysis and results discussion, V. A. S. drafted the manuscript with contributions from all co-authors, the final version was reviewed and proofed by all the authors for publication.

Conflicts of interest

There are no conflicts to declare.

Acknowledgements

All the authors wish to thank Dr Frédéric Jaouen from ICGM, CNRS (Montpellier, France) for providing the catalyst, Dr Blanka Detlefs, Dr Vinod K. Paidi and Timothy Bohdan from ESRF as well as Dr Keyla Teixeira Santos from LEPMI for their assistance and help during the measurements. We also acknowledge the European Synchrotron Radiation Facility for provision of beamtime at ID26 beamline (DOI: 10.15151/ESRF-ES-834188842). K.K. and F.M. gratefully acknowledge the financial support from the French National Research Agency through the DEEP project (grant number ANR-21-CE05-0021).

References

1 H. Bai, J. Feng, D. Liu, P. Zhou, R. Wu, C. T. Kwok, W. F. Ip, W. Feng, X. Sui, H. Liu and H. Pan, *Small*, 2022, 2205638.
2 Y. Sun, S. Sun, H. Yang, S. Xi, J. Gracia and Z. J. Xu, *Adv. Mater.*, 2020, **32**, 1–8.
3 T. Asset and P. Atanassov, *Joule*, 2020, **4**, 33–44.
4 X. Zhang, L. Truong-Phuoc, T. Asset, S. Pronkin and C. Pham-Huu, *ACS Catal.*, 2022, **12**, 13853–13875.
5 J. Li, M. T. Sougrati, A. Zitolo, J. Ablett, I. C. Oguz, T. Mineva, I. Matanovic, P. Atanassov, A. Di Cicco, K. Kumar, L. Dubau, F. Maillard and F. Jaouen, *Nat. Catal.*, 2021, **4**, 10–19.
6 L. Ni, C. Gallenkamp, S. Wagner, E. Bill, V. Krewald and U. I. Kramm, *J. Am. Chem. Soc.*, 2022, **144**(37), 16827–16840.
7 L. Ni, C. Gallenkamp, S. Paul, M. Kübler, P. Theis, S. Chabbra, K. Hofmann, E. Bill, A. Schnegg, B. Albert, V. Krewald and U. I. Kramm, *Adv. Energy Sustain. Res.*, 2021, **2**, 2000064.
8 K. Kumar, L. Dubau, M. Mermoux, J. Li, A. Zitolo, J. Nelayah, F. F. Jaouen, F. Maillard, A. K. Kumar, L. Dubau, M. Mermoux, A. Zitolo, J. Nelayah and F. F. Jaouen, *Angew. Chem., Int. Ed.*, 2020, **59**, 3235–3243.
9 A. Zitolo, V. Goellner, V. Armel, M. T. Sougrati, T. Mineva, L. Stievano, E. Fonda and F. Jaouen, *Nat. Mater.*, 2015, **14**, 937–942.
10 K. Ebner, L. Ni, V. A. Saveleva, B. P. Le Monnier, A. H. Clark, F. Krumeich, M. Nachtegaal, J. S. Luterbacher, U. I. Kramm, T. J. Schmidt and J. Herranz, *Phys. Chem. Chem. Phys.*, 2021, 9147–9157.
11 V. A. Saveleva, K. Kumar, P. Theis, N. S. Salas, U. I. Kramm and P. Glatzel, *ACS Appl. Energy Mater.*, 2023, **6**, 611–616.
12 Q. Jia, N. Ramaswamy, U. Tylus, K. Strickland, J. Li, A. Serov, K. Artyushkova, P. Atanassov, J. Anibal, C. Gumeci, S. C. Barton, M. T. Sougrati, F. Jaouen, B. Halevi and S. Mukerjee, *Nano Energy*, 2016, **29**, 65–82.
13 J. Li, S. Ghoshal, W. Liang, M. T. Sougrati, F. Jaouen, B. Halevi, S. Mckinney, G. Mccool, C. Ma, X. Yuan, Z. F. Ma, S. Mukerjee and Q. Jia, *Energy Environ. Sci.*, 2016, **9**, 2418–2432.
14 L. Osmieri, R. K. Ahluwalia, X. Wang, H. T. Chung, X. Yin, A. J. Kropf, J. Park, D. A. Cullen, K. L. More, P. Zelenay, D. J. Myers and K. C. Neyerlin, *Appl. Catal., B*, 2019, **257**, 117929.
15 K. Ebner, A. H. Clark, V. A. Saveleva, G. Smolentsev, J. Chen, L. Ni, J. Li, A. Zitolo, F. Jaouen, U. I. Kramm, T. J. Schmidt and J. Herranz, *Adv. Energy Mater.*, 2022, **12**, 2103699.
16 M. J. Dzara, K. Artyushkova, M. T. Sougrati, C. Ngo, M. A. Fitzgerald, A. Serov, B. Zulevi, P. Atanassov, F. Jaouen and S. Pylypenko, *J. Phys. Chem. C*, 2020, **124**, 16529–16543.
17 V. A. Saveleva, K. Ebner, J. S. Diercks, S. Unsal Dayanik, L. Artiglia, T. J. Schmidt and J. Herranz, *Insights on Polymer Electrolyte Fuel Cell Degradation of Fe/N/C- Catalysts from X-Ray Photoelectron Spectroscopy*.
18 N. Lee, T. Petrenko, U. Bergmann, F. Neese and S. Debeer, *J. Am. Chem. Soc.*, 2010, **132**, 9715–9727.
19 E. R. Hall, C. J. Pollock, J. Bendix, T. J. Collins, P. Glatzel and S. Debeer, *J. Am. Chem. Soc.*, 2014, **136**, 10076–10084.
20 C. J. Pollock and S. Debeer, *J. Am. Chem. Soc.*, 2011, **133**, 5594–5601.
21 A. V. A. Saveleva, K. Ebner, L. Ni, D. Klose, A. Zitolo, E. Marelli, J. Li, M. Medarde, O. V Safonova, F. Jaouen, U. I. Kramm, J. Thomas and J. Herranz, *Angew. Chem., Int. Ed.*, 2021, **133**, 1–7.
22 S. Lafuerza, A. Carlantuono, M. Retegan and P. Glatzel, *Inorg. Chem.*, 2020, **59**, 12518–12535.
23 P. Glatzel and U. Bergmann, *Coord. Chem. Rev.*, 2005, **249**, 65–95.
24 A. M. March, T. A. Assefa, C. Bressler, G. Doumy, A. Galler, W. Gawelda, E. P. Kanter, Z. Németh, M. Pápai, S. H. Southworth, L. Young and G. Vankó, *J. Phys. Chem. C*, 2015, **119**, 14571–14578.
25 C. J. Pollock and S. DeBeer, *Acc. Chem. Res.*, 2015, **48**, 2967–2975.
26 K. Kumar, P. Gairola, M. Lions, N. Ranjbar-Sahraie, M. Mermoux, L. Dubau, A. Zitolo, F. Jaouen and F. Maillard, *ACS Catal.*, 2018, **8**, 11264–11276.
27 R. Sgarbi, K. Kumar, V. A. Saveleva, L. Dubau, R. Chattot, V. Martin, M. Mermoux, P. Bordet, P. Glatzel, E. A. Ticianelli, F. Jaouen and F. Maillard, *Appl. Catal., B*, 2022, **311**, 121366.
28 K. T. Santos, K. Kumar, L. Dubau, H. Ge, S. Berthon-Fabry, C. S. Vasconcelos, F. Lima, T. Asset, P. Atanassov, V. A. Saveleva, P. Glatzel, X. Li, F. Jaouen and F. Maillard, *J. Power Sources*, 2023, **564**, 232829.
29 A. Zitolo, N. Ranjbar-Sahraie, T. Mineva, J. Li, Q. Jia, S. Stamatin, G. F. Harrington, S. M. Lyth, P. Krtil, S. Mukerjee, E. Fonda and F. Jaouen, *Nat. Commun.*, 2017, **8**, 957–968.

30 S. Lafuerza, M. Retegan, B. Detlefs, R. Chatterjee, V. Yachandra, J. Yano and P. Glatzel, *Nanoscale*, 2020, **12**, 16270–16284.
31 F. Neese, *Wiley Interdiscip. Rev. Comput. Mol. Sci.*, 2018, **8**, 4–9.
32 A. D. Becke, *Phys. Rev. A*, 1988, **38**, 3098–3100.
33 C. van Wüllen, *J. Chem. Phys.*, 1998, **109**, 392–399.
34 F. Weigend and R. Ahlrichs, *Phys. Chem. Chem. Phys.*, 2005, **7**, 3297–3305.
35 F. Neese, *J. Comput. Chem.*, 2003, **24**, 1740–1747.
36 F. Weigend, *Phys. Chem. Chem. Phys.*, 2006, **8**, 1057–1065.
37 S. Grimme, S. Ehrlich and L. Goerigk, *J. Comput. Chem.*, 2011, **32**, 1456–1465.
38 M. Garcia-Ratés and F. Neese, *J. Comput. Chem.*, 2019, **40**, 1816–1828.
39 N. Lee, T. Petrenko, U. Bergmann, F. Neese and S. Debeer, *J. Am. Chem. Soc.*, 2010, **132**, 9715–9727.
40 C. J. Pollock, M. U. Delgado-Jaime, M. Atanasov, F. Neese and S. Debeer, *J. Am. Chem. Soc.*, 2014, **136**, 9453–9463.
41 E. Gallo and P. Glatzel, *Adv. Mater.*, 2014, **26**, 7730–7746.
42 U. Bergmann, C. R. Horne, T. J. Collins, J. M. Workman and S. P. Cramer, *Chem. Phys. Lett.*, 1999, **302**, 119–124.
43 C. J. Pollock, K. M. Lancaster, K. D. Finkelstein and S. Debeer, *Inorg. Chem.*, 2014, **53**, 10378–10385.
44 F. D. Speck, J. H. Kim, G. Bae, S. H. Joo, K. J. J. Mayrhofer, C. H. Choi and S. Cherevko, *J. Am. Chem. Soc.*, 2021, **1**, 1086–1100.
45 J. H. Zagal and M. T. M. Koper, *Angew. Chem., Int. Ed.*, 2016, **55**, 14510–14521.
46 M. Wilke, F. Farges, P. E. Petit, G. E. Brown and F. Martin, *Am. Mineral.*, 2001, **86**, 714–730.
47 Y.-P. Ku, K. Ehelebe, M. Bierling, F. Speck, D. Seeberger, K. Mayrhofer, S. Thiele and S. Cherevko, *J. Am. Chem. Soc.*, 2022, **144**, 21.
48 R. Ma, G. Lin, Q. Ju, W. Tang, G. Chen, Z. Chen, Q. Liu, M. Yang, Y. Lu and J. Wang, *Appl. Catal., B*, 2020, **265**, 118593.
49 H. T. Chung, D. A. Cullen, D. Higgins, B. T. Sneed, E. F. Holby, K. L. More and P. Zelenay, *Science*, 2017, **357**, 479–484.
50 E. F. Holby, G. Wu, P. Zelenay and C. D. Taylor, *J. Phys. Chem. C*, 2014, **118**, 14388–14393.